MATERIALS SCIENCE

Suppressing interfacial nucleation competition through supersaturation regulation for enhanced perovskite film quality and scalability

Gao Zhang[1]†, Bin Ding[2]†, Yong Ding[2,3]†, Yan Liu[1], Changze Yu[1], Lirong Zeng[1], Yao Wang[1], Xin Zhang[1], Meijun Liu[1], Qingyong Tian[4], Bin Fan[4], Qiuju Liu[4], Guanjun Yang[1]*, Mohammad Khaja Nazeeruddin[2]*, Bo Chen[1]*

The growing interest in cost-effective and high-performing perovskite solar cells (PSCs) has driven extensive research. However, the challenge lies in upscaling PSCs while maintaining high performance. This study focuses on achieving uniform and compact perovskite films without pinholes and interfacial voids during upscaling from small PSCs to large-area modules. Competition in nucleation at concavities with various angles on rough-textured substrates during the gas-pumping drying process, coupled with different drying rates across the expansive film, aggravates these issues. Consequently, substrate roughness notably influences the deposition window of compact large-area perovskite films. We propose a supersaturation regulation approach aimed at achieving compact deposition of high-quality perovskite films over large areas. This involves introducing a rapid drying strategy to induce a high-supersaturation state, thereby equalizing nucleation across diverse concavities. This breakthrough enables the production of perovskite photovoltaics with high efficiencies of 25.58, 21.86, and 20.62% with aperture areas of 0.06, 29, and 1160 square centimeters, respectively.

INTRODUCTION

Because of their rapid advancements in performance and cost-effectiveness, perovskite solar cells (PSCs) have gained considerable attention from both the academic and industrial realms (*1*, *2*). Recently, the power conversion efficiency (PCE) of PSCs at a small cell size of <0.1 cm^2 has soared to an impressive 26.1% (*3*–*5*). Nevertheless, compared to traditional silicon solar cells, upscaling PSCs to large-area modules without notable efficiency losses remains a challenge (*6*–*8*), impeding the broader commercialization of this promising photovoltaic technology.

A substantial challenge in upscaling PSCs is the need to produce high-quality perovskite films over large areas while ensuring the absence of pinholes and buried interfacial voids (*9*, *10*). These imperfections can create shunt paths and hinder proper electrical contact, ultimately compromising charge collection efficiency (*11*, *12*). Several strategies have been proposed to address this challenge, primarily focusing on enhancing wettability during the coating process (*13*), engineering intermediate film to facilitate uniform drying (*14*, *15*), reducing the volume shrinkage induced by residual dimethyl sulfoxide (DMSO) during the annealing process (*16*, *17*), and using posthealing techniques (*18*). These strategies effectively prevent the formation of morphological imperfections and inhomogeneous films on a flat substrate.

The impact of substrate roughness on the morphology and upscaling of perovskite films has received relatively limited attention. Transparent conductive oxide (TCO) substrates, such as fluorine-doped tin oxide (FTO) and indium-doped tin oxide (ITO), are commonly used in PSCs, each offering distinct advantages (*19*). In comparison to ITO, the textured FTO substrate is well suited for high-temperature processing applications, reduces reflection losses, extends the length of the optical path (*20*), offers cost-effectiveness, and eliminates the need for rare indium metal (*20*–*24*). Because of the vapor deposition method used in its production, the surface of FTO substrates is textured with greater surface roughness compared to ITO, attributed to the larger grain sizes of FTO spanning from tens to hundreds of nanometers (*23*, *24*). The extent to which the surface roughness of TCO substrates may influence the nucleation and growth process of perovskite films remains insufficiently understood and demands further comprehensive exploration.

Supersaturation, referring to the degree to which the concentration of perovskite precursor exceeds the equilibrium solubility, is a critical parameter in the nucleation and crystal growth process. The supersaturation level is pivotal in determining the critical nucleation energy for both homogeneous and heterogeneous nucleation events, thereby influencing the dynamics of the nucleation process (*25*). In the context of perovskite film formation, the LaMer model, a classical nucleation theory, highlights that nucleation does not commence until the concentration reaches the critical supersaturation level during the drying process (*26*). Despite its importance, a comprehensive understanding of the impact of supersaturation regulation on large-scale perovskite film fabrication remains an area that demands further exploration and investigation.

In this study, we explored the influence of substrate roughness and its interplay with supersaturation on the production of high-quality perovskite films during upscaling. Drying rate discrepancies across the film led to varied supersaturation levels during upscaling, causing nonuniform perovskite films with pinholes and buried interfacial voids in regions with slower drying kinetics. To overcome these challenges, we proposed an innovative supersaturation regulation

[1]State Key Laboratory for Mechanical Behavior of Materials, Xi'an Jiaotong University, Xi'an, Shaanxi 710049, P.R. China. [2]Group for Molecular Engineering of Functional Materials, Institute of Chemical Sciences and Engineering, EPFL VALAIS, Sion 1950, Switzerland. [3]State Key Laboratory of Alternate Electrical Power System with Renewable Energy Sources, North China Electric Power University, Beijing 102206, P. R. China. [4]Kunshan GCL Optoelectronic Materials Co., Ltd., Kunshan, Jiangsu 215300, P.R. China.
*Corresponding author. Email: ygj@mail.xjtu.edu.cn (G.Y.); mdkhaja.nazeeruddin@epfl.ch (M.K.N.); bochen@xjtu.edu.cn (B.C.)
†These authors contributed equally to this work.

strategy aimed at minimizing differences in critical nucleation energies between large-angle and small-angle concavities. This strategy effectively prevented the formation of morphological imperfections at the former, enabling the successful deposition of high-quality perovskite films for large-area modules.

RESULTS

Formation of pinholes and voids during upscaling

We investigated the influence of textured substrate on the uniformity of perovskite films during the scaling-up process, especially during the drying process. The dry films were prepared using our previously reported gas-pumping method (*27*–*29*) at a pressure of 2 kPa and gas flow of 50 liters/min, using a perovskite precursor solution of 1.3 M $Cs_{0.05}MA_{0.05}FA_{0.9}PbI_3$ in dimethylformamide (DMF). For the small sample, we spin-coated the precursor on a textured FTO substrate with a size of 2.5 cm by 2.5 cm. The resulting perovskite film displayed a uniform morphology with black color, regardless of its placement within the drying chamber (Fig. 1A). However, upon transitioning to larger substrates with a dimension of 10 cm by 10 cm while maintaining identical drying conditions, we observed the emergence of nonuniform morphology within the perovskite film by the naked eye (Fig. 1A). The surface changed from a smooth appearance near the gas inlet of the chamber (right side in Fig. 1A) to a rough and hazy surface near the gas outlet (left side in Fig. 1A). Scanning electron microscopy (SEM) images in Fig. 1 (B and G) confirm this difference, revealing an increased presence of pinholes within the perovskite film and interfacial voids at the bottom surface of the perovskite film, progressing from the right side to the left side of the sample. Analysis of the transmittance spectra across the film indicated notable discrepancies in transmittance, which further confirmed the nonuniformity of the deposited film (Fig. 1H). We speculate that the varied film morphology across the film stems from different drying rates across the large sample. Specifically, the higher concentration of accumulated DMF vapor near the gas outlet results in its slower drying rate compared to regions near the gas inlet.

Upon switching the substrate from textured FTO to flat glass, with a corresponding reduction in surface roughness from 20.4 to 2.7 nm (figs. S1 and S2), we achieved uniform film morphology and consistent transmittance spectra for perovskite film deposited on a large substrate of 10 cm by 10 cm (Fig. 1, I and J). This observation underscores the substantial influence of surface roughness on the uniformity of perovskite films during the scaling-up process. To distinguish the influence of the composition of perovskite precursor, we conducted the same experiment using $MAPbI_3$ on substrates with different surface roughnesses (figs. S3 to S5). These experiments also exhibited the same substrate-related effects on the uniformity of small-area and large-area perovskite films.

Impact of surface roughness on morphological imperfections

The wetting angles of FTO, ITO, and glass were measured at 14.7°, 17.6°, and 19.4°, respectively, and wetting angles for all substrates became less than the measurable values after ultraviolet (UV)–O_3 treatment, indicating highly favorable wetting properties (figs. S6 and S7). This suggests that voids and pinholes in dry films on the textured FTO substrate do not manifest during the wetting process but rather during the subsequent drying process. To better understand how substrate roughness affects the emergence of morphological imperfections in perovskite films, we quantified local substrate concave angles beneath the interfacial voids and pinholes. Figure S8 illustrates the use of cross-sectional SEM images for measuring and quantifying the concave angles of the FTO substrate and those beneath the interface voids and pinholes. Statistical data in Fig. 2A were obtained through angle quantification across multiple cross-sectional SEM images, with a total of 100 data points for bare FTO and concavities beneath the interfacial voids and pinholes. For the bare FTO substrate, the concave angles of the rough FTO surface exhibited a nearly symmetrical Gaussian distribution spanning 40° to 160°, with an average angle of approximately 100°. Notably, most voids and pinholes of annealed perovskite film formed at large-angle concavities, particularly within the range of 100° to 160°, with an average angle of approximately 125°. Therefore, substrate roughness leads to the formation of interfacial voids and pinholes primarily at large-angle concavities. This implies that perovskite film nucleation is more favorable at small-angle concavities compared to large-angle concavities.

Furthermore, to demonstrate the nucleation direction of the gas-pumping method, we added saturated poly(methyl methacrylate) (PMMA) polymer into 1.3 M $Cs_{0.05}MA_{0.05}FA_{0.9}PbI_3$ precursor as a nucleation direction indicator. Because of the different saturation levels of PMMA and perovskite in DMF, PMMA precipitates earlier than perovskite during the drying process. For the gas-pumping sample, PMMA is located at the bottom surface of the dry film, while for the antisolvent sample, PMMA is located at the top surface (fig. S9). When the perovskite dry film was peeled off from the FTO substrate, numerous PMMA residues were observed on the FTO substrate for the gas-pumping sample. This indicates that the nucleation direction for the gas-pumping method is from bottom to top. The nucleation direction of the perovskite film during the drying process results from a competition between thermodynamic and kinetic processes. The gas-pumping method under vacuum conditions creates a smaller difference in solvent extraction rates between the top and bottom interfaces compared to the antisolvent method. As illustrated in figs. S10 and S11, the thermodynamic preference for nucleation at the bottom interface still dominates the gas-pumping drying process (*30*), resulting in the bottom-to-top film growth direction. This contrasts with the kinetic preference for nucleation at the top interface observed in the antisolvent method. Moreover, statistical data show grain size compatibility between the perovskite dry film and the FTO substrate (fig. S12), which makes it possible to distinguish the corresponding concavities underneath the interfacial voids and analyze the nucleation behavior between concavities with different angles.

Using classical nucleation theory, we explored the competition between nucleation at large-angle and small-angle concavities. The energy of heterogeneous nucleation (ΔG_{het}) on different local morphology angles (β) on the rough surface is related to the heterogeneous nucleation energy factor, denoted as $f(\beta, \theta)$ (*31*)

$$f(\beta,\theta)=\frac{1}{4}\left[2-3\sin\left(\frac{\beta}{2}+\theta\right)+\sin^3\left(\frac{\beta}{2}+\theta\right)-\cos^3\left(\frac{\beta}{2}+\theta\right)\cot\frac{\beta}{2}\right] \quad (1)$$

$$\Delta G_{het}=\Delta G_{hom}\times f(\beta,\theta)=\left[-\frac{4}{3}\pi r^3\frac{kT}{\Omega}ln(1+\sigma)+4\pi r^2\gamma_{sl}\right]\times f(\beta,\theta) \quad (2)$$

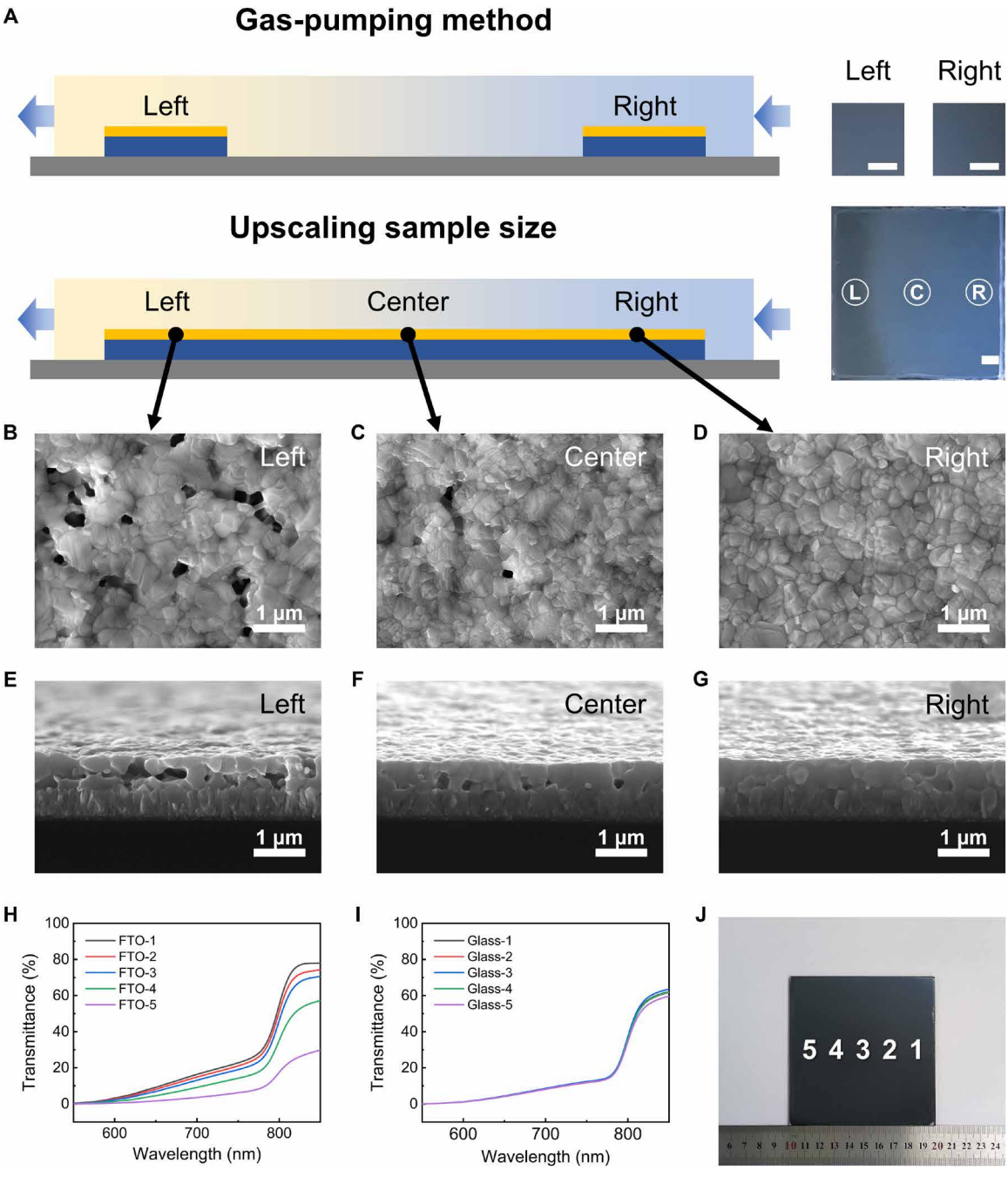

Fig. 1. Formation of pinholes and voids during upscaling. (**A**) Schematic illustration depicting the upscaling process of perovskite film fabrication using the gas-pumping method during the drying process, and photographs of annealed perovskite films deposited on 2.5 cm by 2.5 cm and 10 cm by 10 cm FTO substrate, with a scale bar of 1 cm. The small-area films were dried on the left side and right side of the chamber. (**B** to **D**) Top-view SEM images and (**E** to **G**) cross-sectional SEM images of annealed $Cs_{0.05}MA_{0.05}FA_{0.9}PbI_3$ perovskite films captured at the left ["L" in (A)], center ["C" in (A)], and right ["R" in (A)] regions of the 10 cm by 10 cm FTO substrate, respectively. Transmittance spectra of perovskite films at five different regions of the 10 cm by 10 cm (**H**) FTO and (**I**) glass substrates, as indicated in (J). (**J**) Photograph of 10 cm by 10 cm annealed films on a glass substrate drying through the gas-pumping method, where marks indicate five different locations for UV–visible (vis) absorption measurement.

where θ is the contact angle of the nucleus on the substrate, γ_{sl} is the surface energy of solid-liquid, Ω is monomer volume, r is the radius of the nucleus, k is Boltzmann's constant, and T is temperature. More details about the equations can be found in the Supplementary Materials. As calculated in Fig. 2D, $f(\beta, \theta)$ at large-angle concavities is larger than that at small-angle ones; for instance, the $f(\beta, \theta)$ at 160° concavity is 13.7 times that at 40° concavity when θ is 90°. As a result, considerably higher energy input is required to initiate heterogeneous nucleation at large-angle concavities, owing to the heightened nucleation energy barrier (fig. S13).

The relationship between nucleation rate (J), supersaturation degree (σ), and substrate morphology angle β can be described as (*32*–*35*)

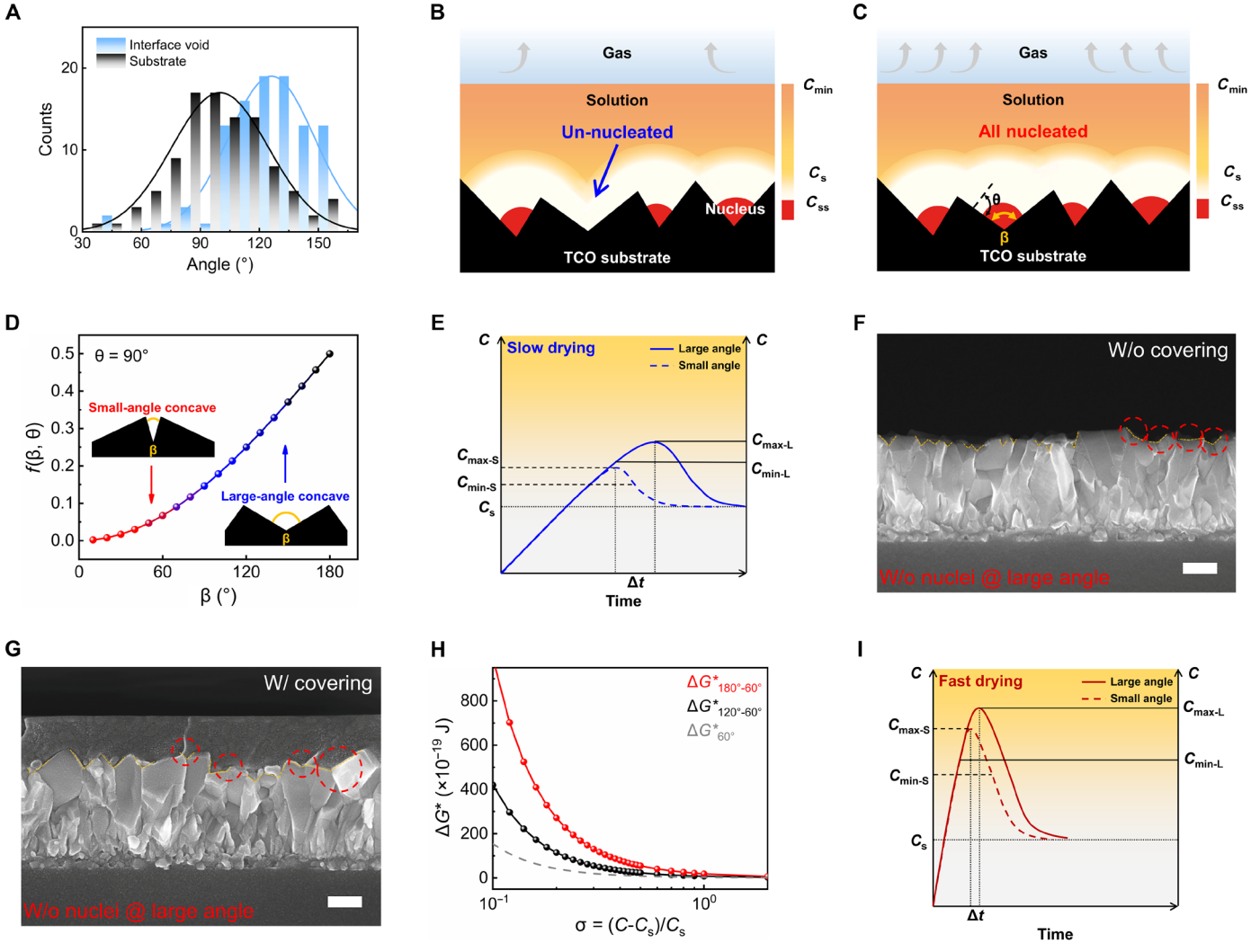

Fig. 2. Impact of substrate roughness and supersaturation on nucleation. (**A**) Statistical data regarding the concave angles of the FTO substrate and the concave angles beneath the interface voids and pinholes. (**B**) Schematic illustration of low supersaturation (LSS) leading to the absence of nucleation at large-angle concavities. (**C**) Schematic illustration of high supersaturation (HSS) leading to nucleation at all concavities. (**D**) Relation between the concave angle and the nucleation energy factor of the nucleus at θ of 90°. (**E**) LaMer curves of slow drying at large and small concave angles. (**F**) Cross-sectional SEM image of the film coated by 0.1 M $Cs_{0.05}MA_{0.05}FA_{0.9}PbI_3$ precursor on rough FTO without covering and (**G**) with covering, showing preferential nucleation at small-angle concavities. Red circles highlight the locations without perovskite nuclei, and yellow lines delineate the concavities on the FTO surface. Scale bars, 200 nm. (**H**) Relationship between supersaturation and the difference in nucleation energy barrier at different angles. (**I**) LaMer curves of fast drying at large and small concave angles.

$$J = \frac{C_s(1+\sigma)kT}{4\pi d^3\eta}\exp\left(-\frac{\Delta G^*_{het}}{kT}\right) = \frac{C_s(1+\sigma)kT}{4\pi d^3\eta}\exp\left(-\frac{\Delta G^*_{hom}\times f(\beta,\theta)}{kT}\right) \quad (3)$$

$$\Delta G^*_{hom} = \frac{16}{3}\pi\frac{\gamma_{sl}^3}{\Delta G_V^2} = \frac{16}{3}\frac{\pi\gamma_{sl}^3\Omega^2}{k^2T^2\ln^2(1+\sigma)} \quad (4)$$

$$\Delta G^*_{het} = \Delta G^*_{hom}\times f(\beta,\theta) \quad (5)$$

where C_s is the saturated concentration of the solution, d is the diameter of the nucleus, η is the viscosity of the solution, ΔG^*_{het} is heterogeneous critical nucleation energy, and ΔG^*_{hom} is homogeneous critical nucleation energy. Figure S14 illustrates the calculated nucleation rate at different concave angles, revealing that nucleation at small-angle concavities requires a lower σ compared to the large-angle counterparts.

The LaMer curves in Fig. 2E show that the minimum concentration for nucleation at large-angle concavities ($C_{min\text{-}L}$) is higher than that at small-angle concavities ($C_{min\text{-}S}$). Consequently, during the drying process, the solution at small-angle concavities reaches the required supersaturation for nucleation before the solution at large-angle concavities. If the maximum concentration at small-angle concavities ($C_{max\text{-}S}$) remains lower than $C_{min\text{-}L}$, nucleation and growth at

small-angle concavities deplete materials from large-angle concavities, thus hindering nucleation in the latter (*26*). This elucidates the competitive dynamics governing the nucleation at small-angle and large-angle concavities.

To pinpoint the initiation points of nucleation, we intentionally reduced the concentration of the perovskite precursor, ensuring that the resulting perovskite film did not entirely cover the textured FTO substrate. By reducing the precursor concentration to 0.1 M under spin coating at 2000 rpm for 10 s, we observed that the tips of the textured FTO grains were left uncovered by perovskite materials after gas-pumping drying (fig. S15). The locations of the perovskite materials can reveal the preferred nucleation sites. Cross-sectional SEM images show that most small-angle concavities had perovskite nuclei, while many large-angle concavities did not (Fig. 2F and fig. S16). We also applied an additional cover layer on the surface of the nuclei to improve the interfacial contrast in the cross-sectional view (Fig. 2G and fig. S16). The statistical results in fig. S17, based on multiple cross-sectional SEM images, demonstrate a competition of nucleation between small-angle and large-angle concavities, with nucleation predominantly initiating from small-angle concavities.

To demonstrate that the uncovered concavities on the rough substrate are not due to nonuniform coating from the spin-coating process of 0.1 M precursor at 2000 rpm, we characterized the thickness of the wet film after spin coating by the weighing method and theoretical calculations (*36*). The wet-film thickness is more than an order of magnitude larger than the roughness of the FTO substrate (Table S1 and figs. S18 and S19), ensuring full coverage of the rough FTO by the wet film and minimizing the impact of FTO roughness on wet-film thickness uniformity. It is the drying process in the gas-pumping chamber that causes preferred nucleation at small-angle sites, resulting in partial coverage of the FTO substrate by the perovskite materials.

Impact of supersaturation inhomogeneity on morphology imperfections

During the drying process of large-area samples, the accumulation of DMF vapor from the inlet to the outlet results in a slower drying rate near the outlet compared to the inlet side. This variation in drying speed leads to differing levels of supersaturation, which subsequently affects the competition of nucleation at concavities with varying angles.

Under fast drying conditions near the inlet, higher degrees of supersaturation reduce the difference in heterogeneous critical nucleation energy $\Delta G^*_{\text{het},\,\beta_L-\beta_S}$ between large-angle and small-angle concavities (Fig. 2H). This is expressed through the equation

$$\Delta G^*_{\text{het},\ \beta_L-\beta_S} = \Delta G^*_{\text{het},\ \beta_L} - \Delta G^*_{\text{het},\ \beta_S} = \frac{16}{3}\frac{\pi\gamma_{sl}^3\Omega^2[f(\beta_L,\theta)-f(\beta_S,\theta)]}{k^2T^2\ln^2(1+\sigma)} \quad (6)$$

Critical nucleation energy is the difference between Gibbs free energy at C_{min} and C_S, and a smaller $\Delta G^*_{\text{het},\,\beta_L-\beta_S}$ during rapid drying indicates smaller difference between $C_{\text{min-S}}$ and $C_{\text{min-L}}$, thus increasing the likelihood of $C_{\text{max-S}}$ surpassing $C_{\text{min-L}}$ (Fig. 2I and fig. S20). As a result, it becomes easier to meet the nucleation requirements for both types of concavities, leading to the formation of dense films without voids or pinholes. Conversely, under slow drying conditions near the outlet, where the drying rate is slowed because of the accumulation of DMF vapor, lower-supersaturation conditions coupled with a larger $\Delta G^*_{\text{het},\,\beta_L-\beta_S}$, as depicted in Fig. 2E and fig. S20, predominantly promote nucleation only at small-angle concavities. When neighboring nuclei are too distant from each other, they consume materials and create pinholes between them. This interplay between surface roughness and supersaturation levels in the formation of morphology imperfections is illustrated in fig. S21.

To confirm the relationship between drying rate and supersaturation levels, we dried the wet film under different pressures and compared the number of formed grains. On the basis of Eqs. 5 and 6), a higher supersaturation level reduces ΔG^*_{het} and $\Delta G^*_{\text{het},\,\beta_L-\beta_S}$ value, facilitating nucleation at more sites and resulting in the formation of more grains with smaller sizes. When the absolute vacuum pressure value reduced from 1 to 0.2 kPa, the average grain size of the unannealed dry film decreased from 125.3 to 82.1 nm, which indicates the formation of more nuclei (fig. S22). This result reveals that rapid drying at a lower pressure value does create a higher supersaturation level. Therefore, rapid drying plays a pivotal role in achieving a fast increase in precursor concentration, leading to a higher supersaturation level before nucleation initiates.

Compact large-area film deposition by supersaturation regulation

To achieve compact perovskite films with intimate interfacial contact without morphological imperfections during upscaling, we propose a supersaturation regulation strategy by rapid drying. According to Eq. 6, we can minimize the nucleation energy difference between different nucleation sites by increasing the supersaturation levels, facilitating the simultaneous initiation of nucleation at various locations with different concave angles.

Under low-supersaturation (LSS) conditions, attained through slow drying at a high absolute pressure of 5 kPa with a gas flow of 25 liters/min, even the perovskite films on small-area FTO substrates of 2.5 cm by 2.5 cm display nonuniform color with the presence of pinholes and interface voids (Fig. 3A and fig. S23). In contrast, using high supersaturation (HSS) via rapid drying at a low absolute pressure of 1 kPa with a gas flow of 25 liters/min during the gas-pumping process results in the formation of uniform and densely packed perovskite films (Fig. 3A and fig. S23). To emphasize the influence of supersaturation on buried interfacial voids, we use an epoxy encapsulant to peel off perovskite films from the FTO substrate (*37*), enabling analysis of the exposed bottom surface morphology. The results reveal that the bottom surface of the perovskite film exhibits numerous voids under the LSS condition, while a compact bottom surface is achieved under the HSS condition (fig. S24). Moreover, both dry films and annealed samples exhibited voids issues under LSS conditions, whereas films prepared under HSS conditions not only eliminated voids in the dry film but also resulted in a compact annealed film (fig. S25). Our findings highlight the effectiveness of the proposed supersaturation strategy in controlling pinholes and voids during the drying stage, with the annealed film exhibiting corresponding improvements to eliminate morphological imperfections.

Besides reducing the absolute pressure, we also used a high gas flow rate to expedite the drying process. By increasing the gas flow from 25 to 50 liters/min, we can achieve uniform perovskite film formation at a high absolute pressure of 5 kPa (Fig. 3A). This underscores the versatility of heightened supersaturation in promoting the deposition of compact perovskite films without morphological imperfections on rough

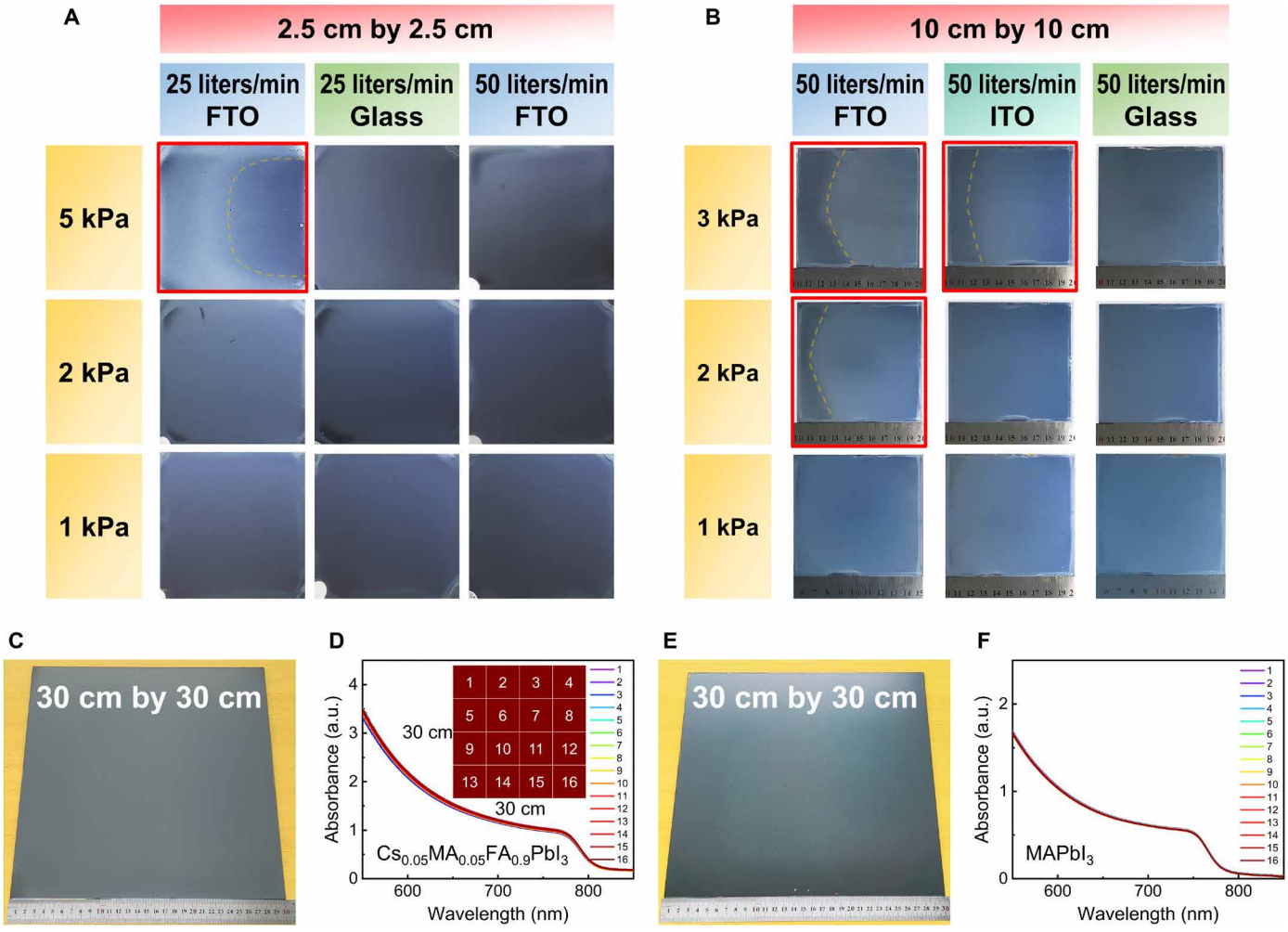

Fig. 3. Achieving uniform large-area perovskite film deposition using HSS through fast drying. Impact of pressure, gas flow, and substrate on (**A**) 2.5 cm by 2.5 cm and (**B**) 10 cm by 10 cm annealed $Cs_{0.05}MA_{0.05}FA_{0.9}PbI_3$ perovskite film deposition via gas-pumping method. The red square highlights conditions leading to a nonuniform film, while the dotted yellow line denotes the boundary between two differently colored annealed films. Photograph of 30 cm by 30 cm annealed (**C**) $Cs_{0.05}MA_{0.05}FA_{0.9}PbI_3$ and (**E**) $MAPbI_3$ perovskite films. UV-vis absorption spectra obtained from 16 different locations of annealed (**D**) $Cs_{0.05}MA_{0.05}FA_{0.9}PbI_3$ and (**F**) $MAPbI_3$ perovskite films, derived by cutting a 30 cm by 30 cm film into 16 individual pieces.

textured FTO substrates. These trends extend to the deposition of various perovskite precursors, such as $MAPbI_3$ with solvent of DMF (fig. S26) and $Cs_{0.05}MA_{0.05}FA_{0.9}PbI_3$ with solvent of DMF:DMSO = 4:1 (fig. S27). A flat-glass substrate eliminates nucleation site competition at different local angles, offering greater tolerance within the drying window for uniform perovskite film formation (Fig. 3A).

Regarding the influence of perovskite precursor concentration, we observed that increasing the concentration does not alleviate the nonuniformity issue during large-area deposition (fig. S28). This is likely because a higher concentration of perovskite precursor may expedite the transition time of the wet film to a supersaturated state, but it does not notably alter the supersaturation level. Consequently, this does not effectively diminish $\Delta G^*_{het,\,\beta_L-\beta_S}$ to achieve the uniform deposition of compact perovskite films.

We expanded our methodology to facilitate the upscaling of perovskite film deposition on the substrate with sizes of 10 cm by 10 cm and 30 cm by 30 cm. For 10 cm by 10 cm FTO substrate, the HSS condition via rapid drying at 1 kPa and 50 liters/min yielded a uniform and densely packed film, while the LSS condition via slow drying at 2 or 3 kPa yielded nonuniform films (Fig. 3B). Furthermore, elevating the gas flow rate from 50 to 100 liters/min facilitated the formation of uniform perovskite film on the 10 cm by 10 cm FTO substrate (fig. S29). We successfully applied this fast-drying HSS approach to deposit uniform perovskite films with dimensions of 30 cm by 30 cm, encompassing various perovskite compositions such as $Cs_{0.05}MA_{0.05}FA_{0.9}PbI_3$ and $MAPbI_3$, as illustrated in Fig. 3 (C and E). To assess film uniformity across large areas, we partitioned the film into 16 segments, conducting individual UV–vis measurements (Fig. 3, D and F). The variation in absorbance at 600 nm is minimal, with an absorption variation of less than 0.6%. In addition, we conducted a comparative analysis of Urbach energies (E_u) across these 16 segments, calculated from UV-vis absorption spectra using $\alpha = \alpha_0 \exp(h\nu/E_u)$, a recognized indicator of photovoltaic material quality (*38*, *39*). The results revealed an average E_u value of 34.16 meV

with a SD of 0.67 meV across various locations (fig. S30). We divided the spin-coated 30 cm by 30 cm large-area sample into 36 individual pieces measuring 5 cm by 5 cm each. Subsequently, we characterized each piece using top-view SEM and cross-sectional SEM images. Across all 36 locations, no pinholes or interfacial voids were observed in the SEM images (figs. S31 to S33). Although there were 5-mm inhomogeneous regions near the substrate edges and corners attributed to the spinning effect, all other areas displayed small thickness deviations within 5% (fig. S34). Particularly, these narrow inhomogeneous regions near the edges were rendered inactive for modules because of edge cleaning during the module fabrication process.

We investigated the impact of substrate roughness, coating methods, and the choice of the charge transport layer (CTL) on nucleation competition, emphasizing the efficacy of the supersaturation regulation strategy across diverse conditions. Compared to the textured FTO substrate, the change of β and $f(\beta, \theta)$ between different sites on the ITO substrate and the flat-glass substrate are smaller (Fig. 2D). Using Eq. 6, the reduced $\Delta f(\beta, \theta)$ and corresponding diminished $\Delta G^*_{het,\ \beta_L-\beta_S}$ on ITO and glass substrates, relative to FTO under equivalent supersaturation levels, led to a narrower disparity between $C_{min\text{-}S}$ and $C_{min\text{-}L}$. This expands the window for compact perovskite film growth on ITO and glass substrates compared to FTO during supersaturation regulation. Under identical drying conditions at 2 kPa and 50 liters/min, the FTO substrate yielded a nonuniform perovskite film, whereas ITO and glass substrates facilitated the formation of a uniform film (Fig. 3B). Furthermore, we observed analogous phenomena and regularities in the blade-coating method for the difference substrates, extending the applicability of our findings beyond spin coating (fig. S35). The conformal deposition of the compact TiO_2@SnO_2 layer using the chemical bath method did not smooth the textured FTO substrate (fig. S36). However, different CTLs alter the supersaturation window for the growth of compact perovskite films in large areas. This is attributed to the diverse contact angles θ of the nucleus on the different CTLs, thereby modifying $\Delta f(\beta, \theta)$ and the corresponding $\Delta G^*_{het,\ \beta_L-\beta_S}$ value under the same change in β values, as illustrated in fig. S37. Nonetheless, the fundamental principle of using an HSS strategy to achieve uniform and compact perovskite films remains unchanged.

Characterization of perovskite films and devices

We thoroughly characterized the effect of the supersaturation regulation approach on charge carrier behavior. Perovskite films prepared under the HSS condition at 1 kPa and 50 liters/min on 2.5 cm by 2.5 cm substrate displayed stronger photoluminescence (PL) intensity and extended carrier lifetimes in comparison to films prepared under LSS condition at 5 kPa (Fig. 4, A and B). This improvement can be attributed to the enhanced film quality through the elimination of pinholes and buried interfacial voids. To investigate the effect of supersaturation regulation on perovskite film trap density, we conducted space charge–limited current (SCLC) measurements using hole-only devices with configuration of FTO/NiO_x/perovskite/Spiro-OMeTAD/Au (Fig. 4C). The HSS device exhibited lower trap-filled limit voltage and lower trap-state density ($V_{TFL} = 0.554$ V; $N_t = 7.92 \times 10^{15}$ cm^{-3}) compared to the LSS device ($V_{TFL} = 0.746$ V; $N_t = 1.07 \times 10^{16}$ cm^{-3}). These findings highlight the positive impact of supersaturation regulation on perovskite film quality and charge carrier behavior.

Figure 4 (D and E) shows the substantially improved photovoltaic performance of PSCs and modules when prepared under HSS conditions compared to LSS conditions. For the small-area inverted PSCs (0.06 cm^2) with the configuration of FTO/TiO_2@SnO_2/perovskite/Spiro-OMeTAD/Au, the current density–voltage (*J-V*) curves of champion devices under different supersaturation conditions are presented in Fig. 4D. Benefiting from the enhanced film quality and better interfacial contact, the HSS device exhibited notable enhancements, with PCE increasing from 21.74 to 25.58%, the open-circuit voltage (V_{OC}) rising from 1.10 to 1.16 V, and the fill factor (FF) increasing from 76.76 to 84.41%. Furthermore, we fabricated perovskite solar modules with an aperture area of 29 cm^2 and eight subcells interconnected in series (Fig. 4E). The champion module achieved an impressive PCE of 21.86%, accompanied by a V_{OC} of 9.28 V, short-circuit current (I_{SC}) of 86.22 mA, and FF of 79.22%. Further details of the photovoltaic performance statistics for 20 perovskite solar modules prepared under HSS conditions are provided in Fig. 4F and detailed parameters are in table S2, demonstrating the high reproducibility of the upscaling strategy under HSS. Subsequently, we fabricated an even larger module with a size of 1160 cm^2 under high-supersaturation drying conditions with perovskite wet film deposited by slot die coating, and we achieved an impressive certified PCE of 20.62% with a V_{OC} of 92.49 V, an I_{SC} of 332 mA, and an FF of 77.9%, providing clear evidence of the scalability of our strategy (figs. S38 and S39).

We conducted long-term stability tests on encapsulated perovskite cells and modules under continuous AM1.5G light-emitting diode light illumination in the air at a relative humidity of ~40 ± 10%. As shown in Fig. 4 (G and H), when tracked at the maximum power point (MPP) with constant illumination, the cell and module prepared under HSS conditions maintained 91 and 83% of their initial efficiency over 1000 hours, outperforming the devices prepared under LSS conditions. This increased stability can be attributed to the reduction in morphological imperfections such as pinholes and interfacial voids, which result in lower defect density and reduced charge recombination. The difference in stabilities between cell and module was ascribed to possible degradation of perovskite film near the scribed line by heat-induced damage and exposure to ambient atmosphere during laser scribing.

DISCUSSION

In conclusion, our study provided a comprehensive understanding of the influence of substrate roughness and supersaturation on formation of high-quality perovskite films for upscaling from small PSCs to large-area perovskite solar modules. We identified that rough substrates with large-angle concavities tend to develop pinholes and voids under LSS conditions during gas-pumping drying process. Furthermore, variations in drying rates across the film introduce different levels of supersaturation, resulting in nonuniform films with morphology imperfections. To overcome these challenges, we introduced a rapid-drying strategy that effectively balances nucleation at different concave angles, thereby preventing the formation of pinholes and interfacial voids. As a result, high-quality perovskite films on a substantial large scale were successfully achieved. This strategy enables the perovskite films with improved morphology, enhanced charge carrier behavior, and reduced trap density. Consequently, it has enabled the fabrication of perovskite solar devices with high efficiencies of 25.58, 21.86, and 20.62% with aperture areas of 0.06, 29, and 1160 cm^2, respectively. The proposed supersaturation regulation strategy aligns well with other ongoing efforts in the field, such as charge transporter layer optimization, additive engineering, and surface passivation. We

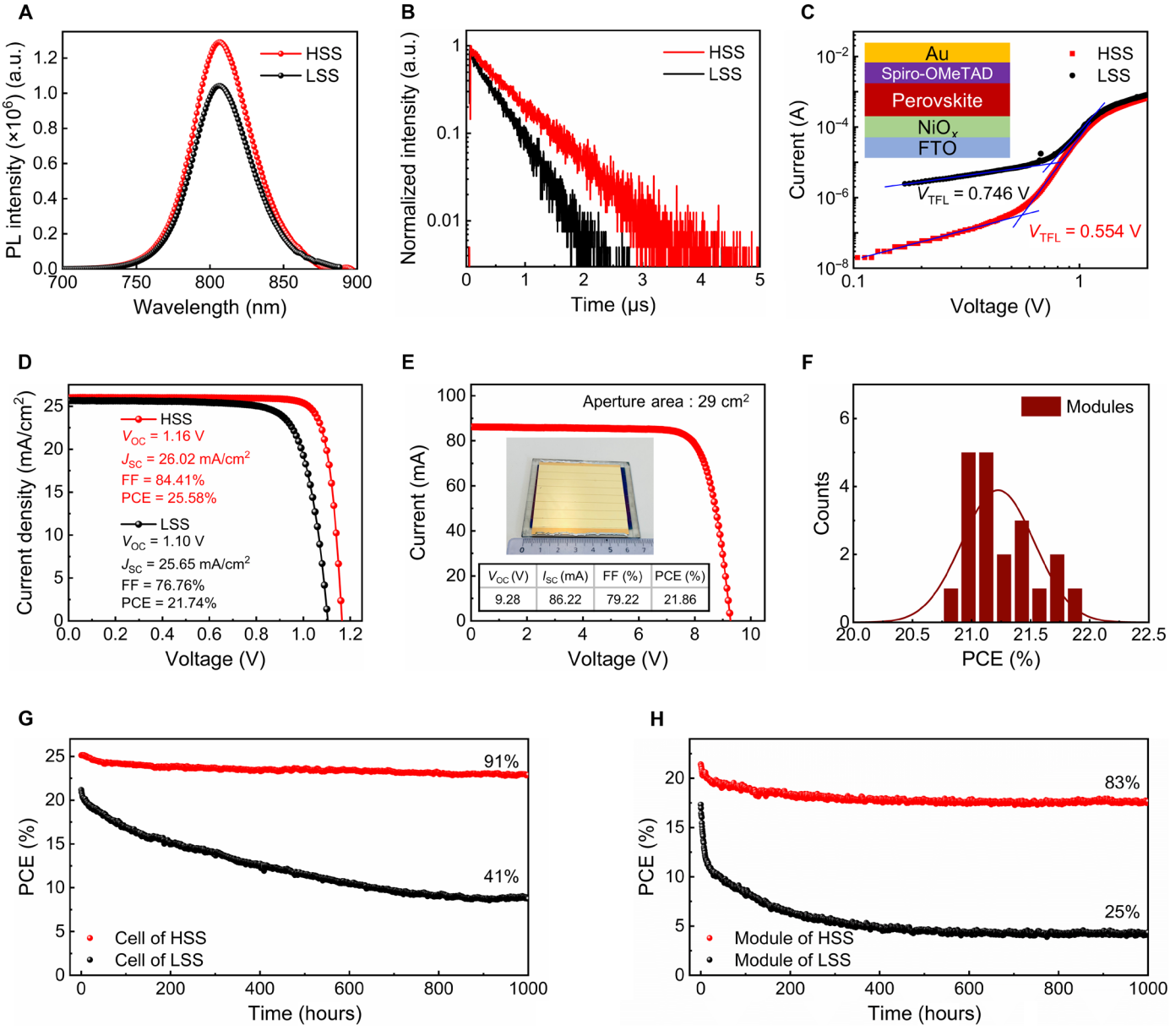

Fig. 4. Performance of PSCs and modules. (**A**) Steady-state PL spectra and (**B**) Time-resolved PL spectra of $Cs_{0.05}MA_{0.05}FA_{0.9}PbI_3$ perovskite films prepared on 2.5 cm by 2.5 cm FTO substrates under HSS (1 kPa and 50 liters/min) and LSS (5 kPa and 50 liters/min). (**C**) SCLC analysis for hole-only devices based on perovskite films prepared under HSS and LSS, with V_{TFL} indicating the trap-filled limit voltage. (**D**) *J-V* curves of champion PSCs with an aperture area of 0.06 cm^2 under simulated 1-sun illumination. (**E**) *I-V* curve of champion perovskite solar module with an aperture area of 29 cm^2 under simulated 1-sun illumination. (**F**) Efficiency distribution for 20 perovskite solar modules. Operational stability of the encapsulated (**G**) 0.06-cm^2 PSCs and (**H**) 29-cm^2 perovskite solar module measured at MPP under a continuous AM1.5G illumination in air.

believe that a synergistic integration of these approaches could pave the way for achieving higher PCEs in both small cells and large-area modules in future endeavors.

MATERIALS AND METHODS

Materials

Lead iodide (PbI_2, 99.99%) was purchased from TCI. Methylammonium iodide (MAI), and formamidinium iodide (FAI) were purchased from GreatCell Solar. Phenethylammonium iodide (PEAI, 99.5%), bis(trifluoromethane)sulfonimide lithium salt (LiTFSI, >99%), 4-tert-butylpyridine (tBP, 96%), and 2,2′,7,7′-tetrakis [*N*, *N*-di(4-methoxyphenyl) amino] 9,9′-spirobifluorene (spiro-OMeTAD, 99.8%) were bought from Xi'an Polymer Light Technology. Cesium chloride (CsCl), PMMA, DMF, DMSO, isopropanol, acetonitrile, and chlorobenzene were purchased from Sigma-Aldrich. FTO glass (TEC, 7 ohm/square), ITO glass (Asahi, 15 ohm per square), and ultraclear glass substrates were purchased from Advanced Election Technology Co., Ltd. Polytetrafluoroethylene (PTFE) filters were purchased from VWR. All the materials were used as received.

Fabrication of PSCs

The patterned FTO substrate was ultrasonically cleaned by sequentially washing with detergent, acetone, ethanol, and deionized water for 20 min, respectively. The compact TiO_2@SnO_2 layer was prepared using a chemical bath method as previously reported (*40*). The $Cs_{0.05}MA_{0.05}FA_{0.9}PbI_3$ perovskite precursor solution (1.3 M) was prepared by adding 659 mg of PbI_2, 10 mg of MAI, 11 mg of CsCl, and 212 mg of FAI in 1-ml mixed solvent of DMF and DMSO in 4:1 volume ratio. The filtered perovskite precursor solution was spin coated onto the TiO_2@SnO_2 substrate at 2000 rpm for 10 s and then transferred to a gas pump chamber. The film was dried under the pressure and flow rate conditions described in the manuscript for 1 min, followed by annealing at 100°C for 30 min. After cooling to room temperature, 60 μl of PEAI solution (3 mg/ml in isopropanol) was dropped on the perovskite layer at 5000 rpm for 30 s. Throughout the process, the ambient temperature was monitored and maintained at 20° ± 5°C, and the relative humidity was maintained at 30 to 45%. Next, the spiro-OMeTAD solution [72.3 mg of spiro-OMeTAD, 30.6 μl of tBP, and 19.5 μl of LiTFSI (520 mg/ml in acetonitrile) in 1 ml of chlorobenzene] was spin coated onto the perovskite film by spin coating at 4000 rpm for 30 s. The spiro-OMeTAD coated sample was then stored in an autodrying cabinet with relative humidity below 10% for 9 hours. Last, a 60-nm gold electrode was deposited onto the spiro-OMeTAD layer via thermal evaporation under a high vacuum ($<5 \times 10^{-4}$ Pa). The PSCs were encapsulated by a glass–glass encapsulation technology combined with an edge seal (UV Curing Sealant, Three Bond) to seal the device under UV light illumination (light-emitting diode flood lamp, DELOLUX 20). The UV light was set at 25% maximum power for 120 s in the glove box to induce the cross-linking in sealant with a glass.

Setup of gas-pumping method

The gas-pumping method setup (*40*) uses a self-built vacuum system with vacuum pumps, vacuum bellows, a sealable chamber, a valve, and a flow meter (with a schematic diagram of the detailed gas-pumping setup in fig. S40). Through the built equipment, the sealed chamber can be quickly pumped and the pressure can be instantly reduced to the set value. The internal pressure of the chamber can be controlled by adjusting the valve in advance. In addition, an adjustable flow meter is added to this basis to control the value of the inlet airflow.

Fabrication of perovskite module and large-area films

The perovskite solar modules, comprising eight subcells connected in series, were fabricated on FTO substrates with dimensions of 6.5 cm by 7.0 cm. The series interconnection of the module was realized by P1, P2, and P3 lines, which were patterned using a laser scribing system with 1064-nm laser at a power of 20 W (Trotec). The FTO substrates were prepatterned P1 lines with a width of 40 μm using 60% laser power under a speed of 300 mm/s, a frequency of 65 kHz, and a pulse duration of 120 ns. The subsequent processes for TiO_2@SnO_2, perovskite film, and spiro-OMeTAD layer were the same as small-area PSCs, where perovskite film was spin coated. The P2 lines, which had a width of 100 μm, were patterned before the Au evaporation process. This was done with an average laser power of 15% under a speed of 1000 mm/s, a frequency of 65 kHz, and a pulse duration of 120 ns. After depositing a 60-nm-thick Au layer, the P3 lines (with a width of 40 μm) were engraved under the same scribing conditions as the P2 lines. The width of the total dead area was approximately 280 μm, resulting in a geometric FF of approximately 95.7%. The perovskite solar modules were encapsulated by the same method and parameters as PSCs. The 30 cm by 30 cm film was prepared by using large-scale spin coating equipment (Leibo-AC300) to achieve liquid film preparation, and the same gas-pumping equipment was built to scale up and dry the film. The blade-coated film was prepared by ZEHNTNER ZAA2300. The blade coater gap was 200 to 300 μm, and the blade coating speed was 20 mm/s. After blade coating, transfer to the gas pump chamber for drying within 3 s. The perovskite film of 1160-cm^2 module was prepared by slot die coating process through homemade slot-die coating machine with a 200-μm gap between the slot-die head and substrate at a speed of 20 mm/s.

Characterization and measurements

The *J-V* curves of PSCs were recorded using a 2400 series source meter from Keithley Instruments. These measurements were conducted under the illumination of a solar simulator (Newport, Class AAA) with an AM 1.5-G filter (Sol3A, Oriel) at a light intensity of 100 mW cm^{-2}. The light source was calibrated using a standard Si reference cell. Each PSC was exposed to light for 10 s before testing. The devices were tested both in forward scan (−0.2 to 1.2 V) and reverse scan (1.2 to −0.2 V) with a step size of 0.01 V and a delay time of 500 ms. The PSCs and modules used metal masks with apertures of 0.06, 29, and 1160 cm^2, respectively. All *J-V* measurements were conducted in an ambient air environment with a temperature of ~25°C and a humidity of 30 to 50%. The stability measurement of encapsulated PSCs and perovskite modules were tested in ambient air environment without cooling at the MPP by using an MPP tracking algorithm under 100 mW cm^{-2}. The devices were covered with an antireflection layer. To investigate the nucleation and growth direction, excess PMMA was added to a 1.3 M perovskite precursor, stirred overnight, and then filtered using a 0.22-μm PTFE filter. For the gas-pumping method, the precursor containing PMMA was spin coated and gas pumped as described above. For the antisolvent method, the precursor containing PMMA was spin coated on the FTO substrate at 2000 rpm for 10 s and 4000 rpm for 30 s. At 20 s of the second step, 200 μl of chlorobenzene was dropped on the spinning film. The surface, cross-sectional, and buried interfacial morphology of perovskite films were examined with a field-emission SEM (FEI VERIOS 460 and Zeiss Sigma 300). Atomic force microscopy measurement was carried out by SPM-9700HT. The UV-vis spectra of the perovskite films were measured in an UV–vis–near infrared spectrophotometer (PE Lambda950). The PL and TRPL decay were carried out using a steady-state–transient fluorescence spectrometer (Edinburgh FLS1000) with the laser diode at a wavelength of 450 nm. SCLC was measured using a Keithley 2400 source meter in dark conditions on hole-only devices with configuration of FTO/NiO_x/perovskite/Spiro-OMeTAD/Au.

Supplementary Materials

This PDF file includes:

Nucleation calculation formula
Figs. S1 to S40
Tables S1 and S2

REFERENCES AND NOTES

1. A. Extance, The reality behind solar power's next star material. *Nature* **570**, 429–433 (2019).
2. Z. Li, T. R. Klein, D. H. Kim, M. Yang, J. J. Berry, M. F. A. M. van Hest, K. Zhu, Scalable fabrication of perovskite solar cells. *Nat. Rev. Mater.* **3**, 18017 (2018).

3. National Renewable Energy Laboratory, Best research-cell efficiency chart; www.nrel.gov/pv/cell-efficiency.html.
4. Y. Zhao, F. Ma, Z. Qu, S. Yu, T. Shen, H. Deng, X. Chu, X. Peng, Y. Yuan, X. Zhang, J. You, Inactive $(PbI_2)_2RbCl$ stabilizes perovskite films for efficient solar cells. *Science* **377**, 531–534 (2022).
5. H. Min, D. Y. Lee, J. Kim, G. Kim, K. S. Lee, J. Kim, M. J. Paik, Y. K. Kim, K. S. Kim, M. G. Kim, T. J. Shin, S. I. Seok, Perovskite solar cells with atomically coherent interlayers on SnO_2 electrodes. *Nature* **598**, 444–450 (2021).
6. Y. Rong, Y. Hu, A. Mei, H. Tan, M. I. Saidaminov, S. I. Seok, M. D. McGehee, E. H. Sargent, H. Han, Challenges for commercializing perovskite solar cells. *Science* **361**, eaat8235 (2018).
7. G. Tong, D. Son, L. K. Ono, Y. Liu, Y. Hu, H. Zhang, A. Jamshaid, L. Qiu, Z. Liu, Y. Qi, Scalable fabrication of >90 cm^2 perovskite solar modules with >1000 h operational stability based on the intermediate phase strategy. *Adv. Energy Mater.* **11**, 2003712 (2021).
8. M. Yang, D. H. Kim, T. R. Klein, Z. Li, M. O. Reese, B. J. Tremolet de Villers, J. J. Berry, M. F. A. M. van Hest, K. Zhu, Highly efficient perovskite solar modules by scalable fabrication and interconnection optimization. *ACS Energy Lett.* **3**, 322–328 (2018).
9. H. Hu, D. B. Ritzer, A. Diercks, Y. Li, R. Singh, P. Fassl, Q. Jin, F. Schackmar, U. W. Paetzold, B. A. Nejand, Void-free buried interface for scalable processing of pin-based $FAPbI_3$ perovskite solar modules. *Joule* **7**, 1574–1592 (2023).
10. H. Huang, Q. Liu, H. Tsai, S. Shrestha, L. Su, P. Chen, Y. Chen, T. Yang, H. Liu, C. Chuang, K. Lin, S. Rwei, W. Nie, L. Wang, A simple one-step method with wide processing window for high-quality perovskite mini-module fabrication. *Joule* **5**, 958–974 (2021).
11. H. Li, G. Xie, X. Wang, S. Li, D. Lin, J. Fang, D. Wang, W. Huang, L. Qiu, Buried interface dielectric layer engineering for highly efficient and stable inverted perovskite solar cells and modules. *Adv. Sci.* **10**, 2300586 (2023).
12. F. H. Isikgor, A. S. Subbiah, M. K. Eswaran, C. T. Howells, A. Babayigit, M. D. Bastiani, E. Yengel, J. Liu, F. Furlan, G. T. Harrison, S. Zhumagali, J. I. Khan, F. Laquai, T. D. Anthopoulos, I. McCulloch, U. Schwingenschlogl, S. D. Wolf, Scaling-up perovskite solar cells on hydrophobic surfaces. *Nano Energy* **81**, 105633 (2021).
13. S. Zhang, F. Ye, X. Wang, R. Chen, H. Zhang, L. Zhan, X. Jiang, Y. Li, X. Ji, S. Liu, M. Yu, F. Yu, Y. Zhang, R. Wu, Z. Liu, Z. Ning, D. Neher, L. Han, Y. Lin, H. Tian, W. Chen, M. Stolterfoht, L. Zhang, W. Zhu, Y. Wu, Minimizing buried interfacial defects for efficient inverted perovskite solar cells. *Science* **380**, 404–409 (2023).
14. W. S. Yang, J. H. Noh, N. J. Jeon, Y. C. Kim, S. Ryu, J. Seo, S. I. Seok, High-performance photovoltaic perovskite layers fabricated through intramolecular exchange. *Science* **348**, 1234–1237 (2015).
15. Y. Deng, C. H. Van Brackle, X. Dai, J. Zhao, B. Chen, J. Huang, Tailoring solvent coordination for high-speed, room-temperature blading of perovskite photovoltaic films. *Sci. Adv.* **5**, eaax7537 (2019).
16. S. Chen, X. Dai, S. Xu, H. Jiao, L. Zhao, J. Huang, Stabilizing perovskite-substrate interfaces for high-performance perovskite modules. *Science* **373**, 902–907 (2021).
17. B. Chen, Z. J. Yu, S. Manzoor, S. Wang, W. Weigand, Z. Yu, G. Yang, Z. Ni, X. Dai, Z. C. Holman, J. Huang, Blade-coated perovskites on textured silicon for 26%-efficient monolithic perovskite/silicon tandem solar cells. *Joule* **4**, 850–864 (2020).
18. Z. Li, X. Wang, Z. Wang, Z. Shao, L. Hao, Y. Rao, C. Chen, D. Liu, Q. Zhao, X. Sun, C. Gao, B. Zhang, X. Wang, L. Wang, G. Cui, S. Pang, Ammonia for post-healing of formamidinium-based Perovskite films. *Nat. Commun.* **13**, 4417 (2022).
19. R. M. Pasquarelli, D. S. Ginley, R. O'Hayre, Solution processing of transparent conductors: From flask to film. *Chem. Soc. Rev.* **40**, 5406–5441 (2011).
20. S. M. Park, M. Wei, N. Lempesis, W. Yu, T. Hossain, L. Agosta, V. Carnevali, H. R. Atapattu, P. Serles, F. T. Eickemeyer, H. Shin, M. Vafaie, D. Choi, K. Darabi, E. D. Jung, Y. Yang, D. B. Kim, S. M. Zakeeruddin, B. Chen, A. Amassian, T. Filleter, M. G. Kanatzidis, K. R. Graham, L. Xiao, U. Rothlisberger, M. Grätzel, E. H. Sargent, Low-loss contacts on textured substrates for inverted perovskite solar cells. *Nature* **624**, 289–294 (2023).
21. E. Fortunato, D. Ginley, H. Hosono, D. C. Paine, Transparent conducting oxides for photovoltaics. *MRS Bull.* **32**, 242–247 (2007).
22. S. M. Park, M. Wei, J. Xu, H. R. Atapattu, F. T. Eickemeyer, K. Darabi, L. Grater, Y. Yang, C. Liu, S. Teale, B. Chen, H. Chen, T. Wang, L. Zeng, A. Maxwell, Z. Wang, K. R. Rao, Z. Cai, S. M. Zakeeruddin, J. T. Pham, C. M. Risko, A. Amassian, M. G. Kanatzidis, K. R. Graham, M. Grätzel, E. H. Sargent, Engineering ligand reactivity enables high-temperature operation of stable perovskite solar cells. *Science* **381**, 209–215 (2023).
23. R. A. Kerner, B. P. Rand, Electrochemical and thermal etching of indium tin oxide by solid-state hybrid organic-inorganic perovskites. *ACS Appl. Energy Mater.* **2**, 6097–6101 (2019).
24. M. Kim, J. Jeong, H. Lu, T. K. Lee, F. T. Eickemeyer, Y. Liu, I. W. Choi, S. J. Choi, Y. Jo, H.-B. Kim, S. I. Mo, Y. K. Kim, H. Lee, N. G. An, S. Cho, W. R. Tress, S. M. Zakeeruddin, A. Hagfeldt, J. Y. Kim, M. Grätzel, D. S. Kim, Conformal quantum dot–SnO_2 layers as electron transporters for efficient perovskite solar cells. *Science* **375**, 302–306 (2022).
25. V. K. LaMer, Kinetics in phase transitions. *Ind. Eng. Chem.* **44**, 1270–1277 (1952).
26. V. K. LaMer, R. H. Dinegar, Theory, production and mechanism of formation of monodispersed hydrosols. *J. Am. Chem. Soc.* **72**, 4847–4854 (1950).
27. B. Ding, L. Gao, L. Liang, Q. Chu, X. Song, Y. Li, G. Yang, B. Fan, M. Wang, C. Li, C. Li, Facile and scalable fabrication of highly efficient lead iodide perovskite thin-film solar cells in air using gas pump method. *ACS Appl. Mater. Interfaces.* **8**, 20067–20073 (2016).
28. B. Ding, Y. Li, S. Huang, Q. Chu, C. Li, C. Li, G. Yang, Material nucleation/growth competition tuning towards highly reproducible planar perovskite solar cells with efficiency exceeding 20%. *J. Mater. Chem. A* **5**, 6840–6848 (2017).
29. X. Li, Z. Li, G. Zhang, G. Yang, Lead-free perovskite $[H_3NC_6H_4NH_3]CuBr_4$ with both a bandgap of 1.43 eV and excellent stability. *J. Mater. Chem. A* **8**, 5484–5488 (2020).
30. C. Zhang, W. Lu, Y. Xu, K. Zeng, G. W. Ho, Mechanistic formulation of inorganic membranes at the air-liquid interface. *Nature* **616**, 293–299 (2023).
31. Y. Li, B. Ding, Q. Chu, G. Yang, M. Wang, C. Li, C. Li, Ultra-high open-circuit voltage of perovskite solar cells induced by nucleation thermodynamics on rough substrates. *Sci. Rep.* **7**, 46141 (2017).
32. G. Cao, *Nanostructures & Nanomaterials: Synthesis, Properties & Applications* (Imperial College Press, 2004).
33. A. A. Petrov, A. A. Ordinartsev, S. A. Fateev, E. A. Goodilin, A. B. Tarasov, Solubility of hybrid halide perovskites in DMF and DMSO. *Molecules* **26**, 7541 (2021).
34. D. Brian, M. R. Ahmadian-Yazdi, C. Barratt, M. Eslamian, Impact dynamics and deposition of perovskite droplets on PEDOT:PSS and TiO_2 coated glass substrates. *Exp. Therm. Fluid Sci.* **105**, 181–190 (2019).
35. M. R. Ahmadian-Yazdi, A. Rahimzadeh, Z. Chouqi, Y. Miao, M. Eslamian, Viscosity, surface tension, density and contact angle of selected PbI_2, $PbCl_2$ and methylammonium lead halide perovskite solutions used in perovskite solar cells. *AIP Adv.* **8**, 025109 (2018).
36. D. Meyerhofer, Characteristics of resist films produced by spinning. *J. Appl. Phys.* **49**, 3993–3997 (1978).
37. X. Yang, D. Luo, Y. Xiang, L. Zhao, M. Anaya, Y. Shen, J. Wu, W. Yang, Y. Chiang, Y. Tu, R. Su, Q. Hu, H. Yu, G. Shao, W. Huang, T. P. Russell, Q. Gong, S. D. Stranks, W. Zhang, R. Zhu, Buried interfaces in halide perovskite photovoltaics. *Adv. Mater.* **33**, 2006435 (2021).
38. J. Park, J. Kim, H. S. Yun, M. J. Paik, E. Noh, H. J. Mun, M. G. Kim, T. J. Shin, S. I. Seok, Controlled growth of perovskite layers with volatile alkylammonium chlorides. *Nature* **616**, 724–730 (2023).
39. B. Subedi, C. Li, C. Chen, D. Liu, M. M. Junda, Z. Song, Y. Yan, N. J. Podraza, Urbach energy and open-circuit voltage deficit for mixed anion–cation perovskite solar cells. *ACS Appl. Mater. Interfaces* **14**, 7796–7804 (2022).
40. B. Ding, S. Huang, Q. Chu, Y. Li, C. Li, C. Li, G. Yang, Low-temperature SnO_2-modified TiO_2 yields record efficiency for normal planar perovskite solar modules. *J. Mater. Chem. A* **6**, 10233–10242 (2018).

Acknowledgments: The authors thank C.Y. Liang, F.C. Tan, D. He, and J.W. Wang at the Instrument Analysis Center of Xi'an Jiaotong University for assistance with the UV-vis, PL, and SEM testing. We also acknowledge the beneficial support from senior engineer W. Wang from the School of Materials Science and Engineering, Xi'an Jiaotong University. **Funding:** This work was financially supported by the National Key R&D Program of China (grant no. 2019YFB1503200), the National Natural Science Foundation of China (grant no. 52273273), and the National Program for Support of Top-notch Young Professionals. **Author contributions:** G.Z., G.Y., and B.C. conceived the idea. B.C., G.Y., and M.K.N. designed and supervised the research. G.Z. performed the SEM, UV-vis, PL, and TRPL characterization. G.Z. and C.Y. fabricated large-area films. B.D., Y.D., and G.Z. fabricated high-performance PSCs and modules. Q.T., B.F., and Q.L. fabricated large-size modules. G.Z. and B.C. wrote the paper, and all authors reviewed the paper. **Competing interests:** The authors declare that they have no competing interests. **Data and materials availability:** All data needed to evaluate the conclusions in the paper are present in the paper and/or the Supplementary Materials.

Submitted 31 October 2023
Accepted 1 July 2024
Published 7 August 2024
10.1126/sciadv.adl6398